DOI 10.1007/s10946-024-10192-8
Journal of Russian Laser Research, Volume 45, Number 1, January, 2024

RESEARCH ON GHOST IMAGING METHOD BASED ON BINOCULAR VISION MATCHING FUSION

Hualong Ye,[1] Daidou Guo,[2*] and Tongxu Xu[1]

[1] *School of Electrical and Information Engineering*
Changshu Institute of Technology
Suzhou 215500, China

[2] *University of Shanghai for Science and Technology*
Shanghai 200093, China

[*]Corresponding author e-mail: 2367272689@qq.com

Abstract

In order to meet the visual characteristics of human eyes, in this paper, we propose a ghost imaging method based on binocular vision matching fusion. The imaging process of the left-eye camera and the right-eye camera in binocular vision system is realized, using ghost imaging algorithm, and its weak signal imaging characteristics can effectively compensate the parallax between the left-eye camera and the right-eye camera. The Speeded Up Robust Features algorithm is used to match the feature points of the two sub-images. Combined with the fusion algorithm of New Sum of Modified Laplacian, the two sub-images after registration are fused to obtain a clearer image. Whether from the visual perception (human vision) or objective analysis (CC, SSIM, IE, RMSE, PSNR, and BER), it can be proved that the proposed scheme has better image quality, better fidelity and robustness, and is closer to the ideal image, which provides a new method for binocular vision imaging technology.

Keywords: binocular vision imaging, ghost imaging, feature matching, fusion reconstruction.

1. Introduction

In recent years, with the development of quantum imaging and related disciplines, imaging technology based on binocular vision has attracted more and more attention. Due to its simple equipment, low cost, convenient operation, and potential of real-time and online imaging, binocular vision imaging technology has been widely used in many fields such as industrial production, object recognition, robot automatic navigation, unmanned driving, and aerospace [1, 2]. Factors affecting the imaging accuracy of binocular vision system include imaging algorithm of the left-eye camera and the right-eye camera, extraction and matching of feature points, parameter selection of system structure, etc. [3, 4]. Most binocular vision systems are constructed by human experience, and there are few reference materials. For example, Z. Xiao [5] theoretically analyzed the effects of camera calibration, lens parameters, and system structure parameters on the binocular vision measurement system. Y. Lu [6] comprehensively analyzed the effects of system structure parameters and camera calibration parameters on the positioning accuracy of binocular vision system. C. Bi [7] derived the expressions of structural parameters and measurement errors such as baseline spacing, camera focal length, object distance, and pixel error through the formula. Some foreign scholars have also conducted researches on this issue. F. Fahimeh [8] analyzed the influence of parameters such as baseline length, focal length, and pixel size on errors through simulation.

Manuscript submitted by the authors in English on October 20, 2023.

Ghost imaging is a new imaging method that utilizes quantum entanglement properties or spatial intensity correlation to obtain object imaging. From the prospective of information theory, ghost imaging technology breaks through the traditional imaging concept of linear optics [9–12], has the characteristics of super noise resistance and high resolution imaging as well as the characteristics of imaging weak signal under harsh optical conditions. In 1988, D. N. Klyshko [13] proposed ghost imaging based on the photon-pair entanglement behavior, and its object-image separation mode has attracted the attention of most scholars. In 2008, J. Shapiro [14] used a spatial light modulator (SLM) to preset the illumination speckle field on an object and realized computational ghost imaging with only a single pixel detector. In 2013, C. Luo [15] realized the improvement of image resolution by modulating Gaussian light source with double cosine function, and derived the calculation formula of point diffusion function. In 2015, Z. Zhang [16] used sinusoidal mode to encode light field, which significantly reduced the ghost imaging of reconstruction time and improved the anti-noise ability. In 2018, D. Shi [17] proposed a novel polarization-multiplexing ghost-imaging technology, which used a single detector to acquire multiple polarization information to recover the fused images containing different polarization information. In 2019, L. Zhang [18] applied ghost imaging to the encoding and transmission process of information, which improved the compressibility of encoded images, avoided the difficulty for attackers to decipher them, and enhanced the anti-interference and anti-interception capabilities. In 2022, D. Zhang's research group [19] proposed a high-resolution ghost imaging reconstruction method based on SURF-NSML to obtain clear images after registration fusion of low-resolution images obtained by the system. In order to make ghost imaging better practical, domestic and foreign scholars have conducted in-depth studies [20–23].

Based on the mentioned results, in this paper, we propose a ghost imaging method based on binocular vision matching fusion. First, the imaging process of binocular vision is simulated by ghost imaging algorithm. The weak signal imaging characteristics of ghost imaging can effectively compensate the parallax between the left-eye camera and the right-eye camera. We use the Speeded Up Robust Features (SURF) algorithm to extract the feature points of the collected left and right images and match the feature points to obtain the coordinate values of the matching points. Finally, we employ the New Sum of Modified Laplacian (NSML) fusion algorithm to fuse the two registered sub-images for obtaining a reconstructed image, which is very close to the ideal image.

2. Research Methods

2.1. Ghost Imaging

Ghost imaging is a new optical imaging method that utilizes quantum entanglement properties or spatial intensity correlation to obtain object imaging. Different from the imaging mode of traditional optical imaging, ghost imaging can realize nonlocal imaging that traditional optical imaging cannot. The principle of ghost imaging is shown in Fig. 1.

It is assumed that $\varphi_i(x, y)$ follows a uniform distribution over $[0, 2\pi]$. A spatially correlated laser beam is illuminated vertically on the spatial light modulator SLM, which modulates the phase of the

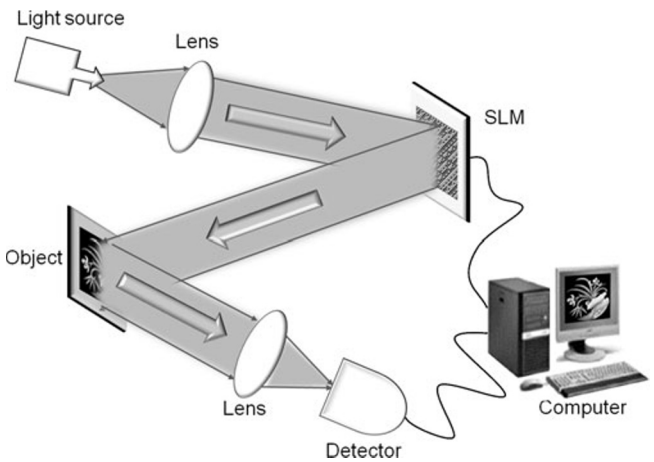

Fig. 1. Optical schematics based on ghost imaging.

light according to the input phase picture $\varphi_i(x, y)$, and the light field distribution is $\{I_i(x, y)\}$. The random light spot generated after SLM is irradiated on the object $T(x, y)$ to be imaged, and the light intensity value of the object diffraction is collected by the detector and calculated to get the light intensity value B_i. According to the Fresnel propagation function, the calculation formula reads

$$B_i = \int I_i(x, y)T(x, y)\ dx\, dy, \qquad \text{with} \qquad I_i(x, y) = |E_{in}(x, y) \exp[j\varphi_i(x, y)] \otimes h_s(x, y)| \tag{1}$$

being the Fresnel diffraction function propagated over a distance z, where $\otimes$ is the convolution operation. The process expression of reconstructing the original information of the object, using the correlation function, is as follows:

$$T_{\mathrm{GI}}(x, y) = \frac{1}{N} \sum_{i=1}^{N} (B_i - \langle B \rangle)\, I_i(x, y), \tag{2}$$

where $\langle B \rangle$ represents the average light intensity value, and N represents the collection times.

2.2. Mechanism of Ghost Imaging Based on Binocular Vision Matching Fusion

In Fig. 2, we show the principle of the ghost imaging method based on binocular vision matching fusion. First, the imaging process of binocular vision is simulated by ghost imaging algorithm. Then, we use the SURF algorithm to register the two camera images collected. Finally, using the NSML fusion algorithm, the two registered sub-images are fused to obtain an ideal image, which is very similar to the target object. The specific steps are as follows:

Step 1. Obtain Images. First, the imaging process of binocular vision is simulated by ghost imaging algorithm. The illumination speckle after SLM modulation is irradiated on the target object $T(x, y)$ to be imaged, and the light field distribution is $\{I_i(x, y)\}$. The light intensity value reflected by the object is collected by detector 1 and detector 2 in the binocular camera, and the light intensity value is B_i. The image information on the object is reconstructed, using the correlation function in the computer. The calculation formulas read

$$B_{1i} = \int I_{1i}(x, y)T(x, y)\ dx\, dy, \qquad B_{2i} = \int I_{2i}(x, y)T(x, y)\ dx\, dy, \tag{3}$$

$$T_1(x, y) = \frac{1}{N} \sum_{i=1}^{N} (B_{1i} - \langle B_1 \rangle)\, I_{1i}(x, y), \qquad T_2(x, y) = \frac{1}{N} \sum_{i=1}^{N} (B_{2i} - \langle B_2 \rangle)\, I_{2i}(x, y). \tag{4}$$

In the binocular vision system in this paper, information collected by the left-eye camera and the right-eye camera is calculated by the ghost imaging algorithm to obtain two sub-images T_1 and T_2.

Step 2. Image Registration. In the process of image registration fusion, in order to perform a sufficiently accurate shift estimation between images, we use the SURF algorithm to register the two sub-images T_1 and T_2; see Fig. 3. SURF determines the matching degree by calculating the Euclidean distance between two feature points [24]. At the same time, the judgment of Hessian matrix traces is added. The detection of SURF feature points is based on the scale-space theory. For the point at

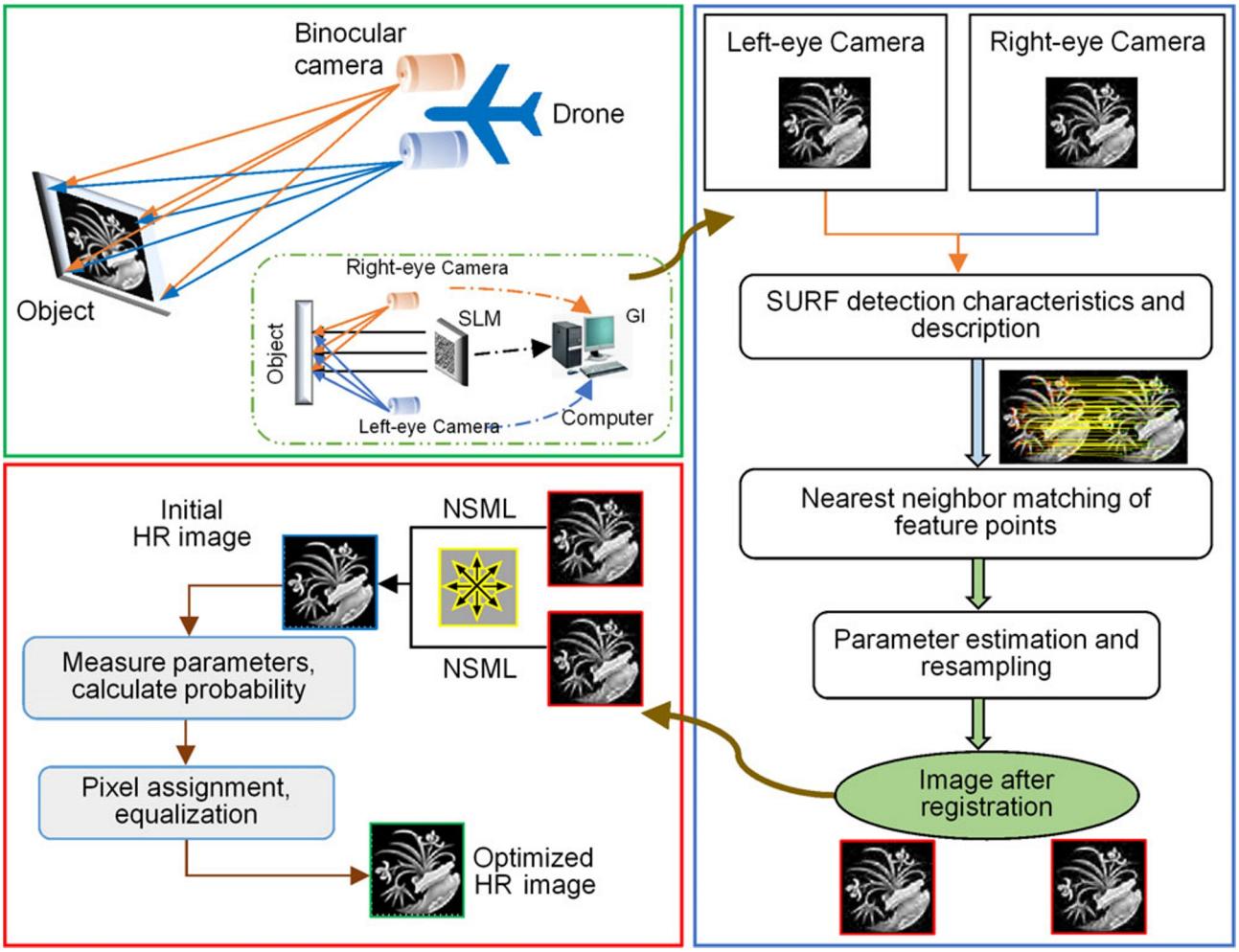

Fig. 2. Schematic of ghost imaging method based on binocular vision matching fusion.

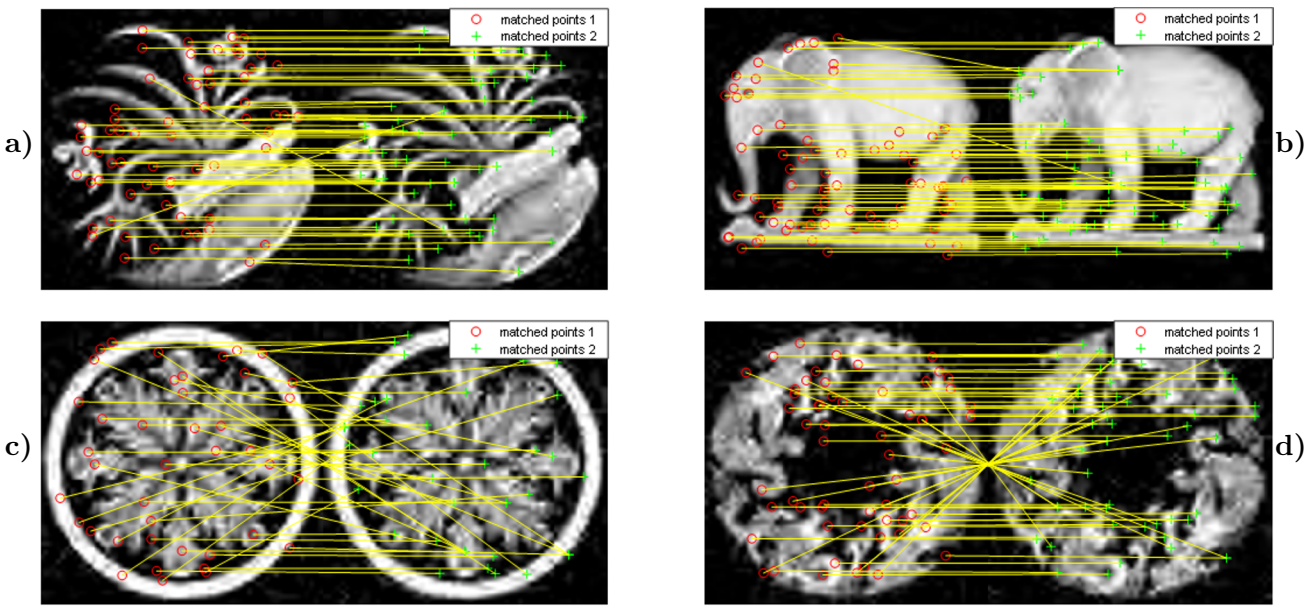

Fig. 3. Feature matching effect of the SURF method.

$\bar{x} = (x, y)$ in image $T(x, y)$, the Hessian matrix expression on scale δ is as follows:

$$H = \begin{bmatrix} L_{xx}(\bar{x}, \delta) & L_{xy}(\bar{x}, \delta) \\ L_{xy}(\bar{x}, \delta) & L_{yy}(\bar{x}, \delta) \end{bmatrix}. \tag{5}$$

By constructing a scale image pyramid and using Hessian matrix to find the extreme value, we select candidate feature points and then carry out interpolation operations in the scale space and the image space [25] to obtain stable feature point positions and scale values. In order to ensure rotation invariability, the Haar wavelet response of points in the neighborhood with radius of $6\,s$ (s is the scale value, where the feature point is located) is first calculated with the feature point as the center, and the response within the range of 60° is combined to form a new vector. The direction of the longest vector is selected as the main direction of the feature point. Take the feature point as the center, rotate the coordinate axis to the main direction, select a square area with a side length of $20\,s$ according to the main direction, divide the window area into 4×4 sub-regions, calculate the wavelet response, then add the response of each sub-region and the absolute value of the response to form a description vector, and then normalize the vector.

After the feature points of the two images to be registered are obtained by the SURF method, we use the nearest neighbor vector matching method to calculate the Euclidian distance for all the feature points, and all potential matching pairs are found without additional information calculation. At last, the RANSAC and the least square method are combined to calculate the transformation relationship between images and remove the influence of mismatching. The registration images are re-sampled to obtain the registration results in the same coordinate system.

Step 3. Image Fusion. After the registration of the two sub-images, we adopt here the NSML image fusion algorithm in order to obtain the fusion effect, with better visual characteristics and richer and more prominent details [26]. On the basis of traditional SML calculating the only horizontal and vertical directions of the variable step size Laplacian value of each pixel, the algorithm adds four directions on the diagonal. The algorithm is defined as follows:

$$\begin{aligned} \mathrm{ML}\,(x, y) \;=\; & |2\,T(x, y) - T(x - \varepsilon, y) - T(x + \varepsilon, y)| + |2\,T(x, y) - T(x, y - \varepsilon) - T(x, y + \varepsilon)| \\ & + |1.4\,T(x, y) - 0.7\,T(x - \varepsilon, y - vep) - 0.7\,T(x + \varepsilon, y + \varepsilon)| + |1.4\,T(x, y) \\ & - 0.7\,T(x + \varepsilon, y - vep) - 0.7\,T(x - \varepsilon, y + \varepsilon)|, \end{aligned} \tag{6}$$

$$\mathrm{NSML}(x, y) = \sum_i \sum_j \mathrm{ML}(i, j), \tag{7}$$

where ε is a variable step parameter. The NSML fusion algorithm has excellent resolution discrimination ability, and the higher the resolution of the image, the larger the corresponding NSML value. Assuming that $T_1(x, y)$ and $T_2(x, y)$ respectively represent the pixel values corresponding to the two sub-images at the same position, $\mathrm{NSML}_1(x, y)$ and $\mathrm{NSML}_2(x, y)$ respectively represent the NSML sharpness of $T_1(x, y)$ and $T_2(x, y)$, the fusion rule based on NSML algorithm is as follows:

$$T'(x, y) = \begin{cases} T_1(x, y), & \mathrm{NSML}_1(x, y) \geq \mathrm{NSML}_2(x, y), \\ T_2(x, y), & \mathrm{NSML}_2(x, y) > \mathrm{NSML}_1(x, y). \end{cases} \tag{8}$$

3. Results and Analysis

In the research process, four images (Picture A, Picture B, Picture C, and Picture D) are selected as the original target images, respectively. In Fig. 4, we show the sub-images reconstructed by the left-eye camera, the right-eye camera, and the imaging effects of binocular cameras under different sampling rates.

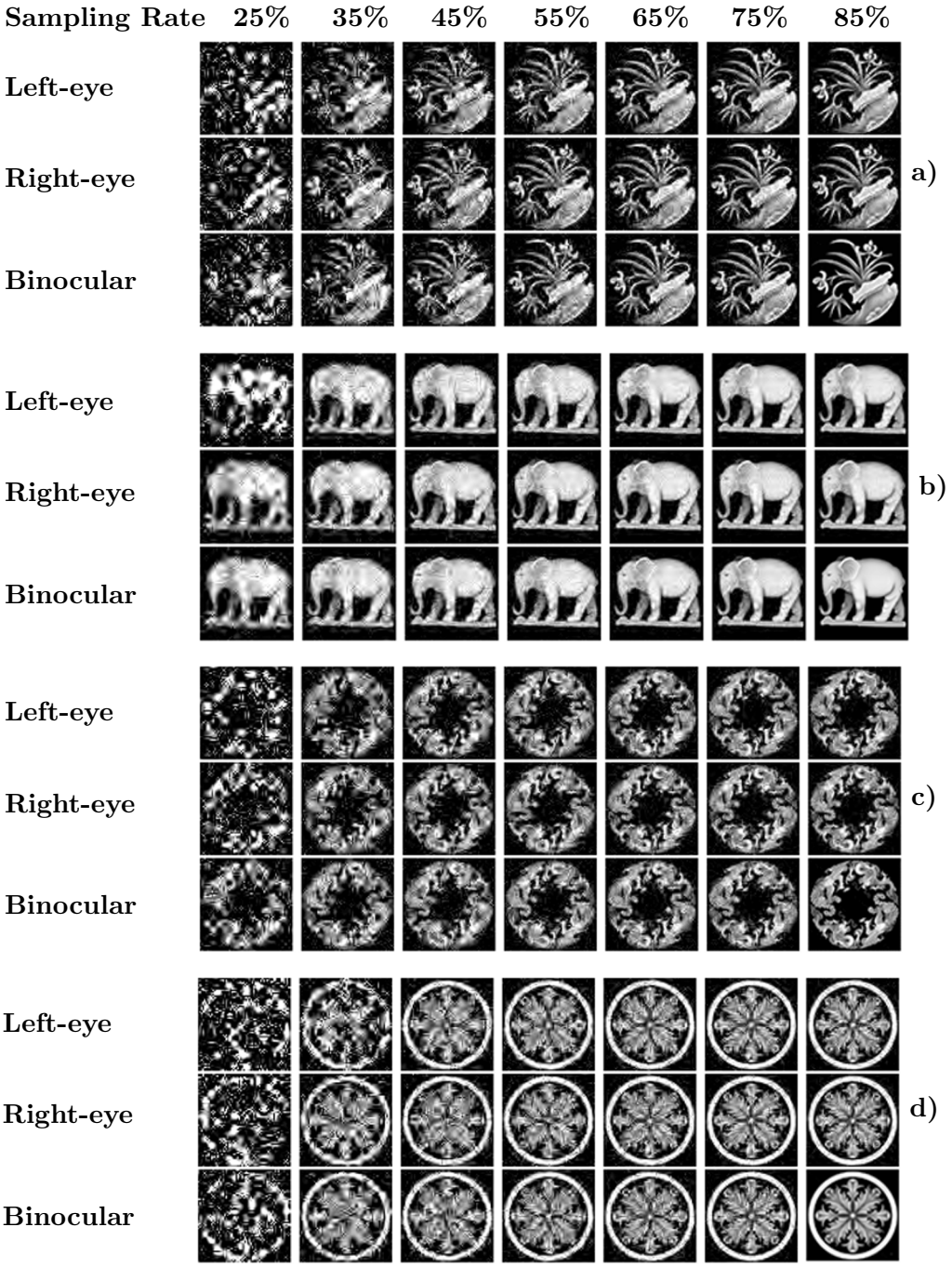

Fig. 4. Imaging effects of the single camera and the binocular camera; here, Picture A imaging effect (a), Picture B imaging effect (b), Picture C imaging effect (c), and Picture D imaging effect (d).

Through comparison, it can be intuitively found that, under the same sampling rate, the imaging quality of the imaging scheme is better and clearer. In order to fully analyze the imaging effect of this scheme, we use six common image evaluation indices, such as correlation coefficient, structural similarity, information entropy, root mean square error, peak signal-to-noise ratio and bit error rate, to verify and analyze.

3.1. Correlation Coefficient

To study the anti-interference ability of the reconstruction scheme, we use the correlation coefficient (CC). In the process of information transmission, noise attack is inevitable, and noise affects the quality of information transmission. The greater the CC value, the greater the correlation degree and the stronger the anti-interference ability. If x and y represent the pixel values of two adjacent pixels in the image information, respectively, then its calculation formulas read

$$\begin{cases} E(x) = \dfrac{1}{N}\sum\limits_{i=1}^{N} x_i, \qquad D(x) = \dfrac{1}{N}\sum\limits_{i=1}^{N}[x_i - E(x)]^2, \\ \operatorname{cov}(x,y) = \dfrac{1}{N}\sum\limits_{i=1}^{N}[x_i - E(x)][y_i - E(y)], \qquad \mathrm{CC} = \dfrac{\operatorname{cov}(x,y)}{\sqrt{D(x)}\sqrt{D(y)}}. \end{cases} \tag{9}$$

In Fig. 5, we show the comparison of CC values of the imaging results of the four target images selected by the left-eye camera, the right-eye camera, and binocular camera at different sampling rates. Here, the gray curve and the red curve represent the CC value change of the reconstructed image of the left-eye camera and the right-eye camera, respectively, and the blue curve represents the CC change of the image reconstructed by binocular camera fusion. From the curve change trend, one can see that

(1) With increase in the sampling rate, the CC value becomes larger and larger; that is, the imaging quality becomes higher and higher, and the anti-interference ability becomes stronger and stronger.

(2) For any kind of target image, the binocular vision fusion imaging CC value based on the proposed scheme is larger than that of the imaging CC value of the left-eye camera and the right-eye camera, indicating that the imaging scheme has better anti-interference ability, better imaging quality, and is closer to the ideal image information.

3.2. Structural Similarity

To verify the feasibility of the scheme, we use the structural similarity (SSIM). It is a method to measure the similarity between the reconstructed image and the ideal image, which is consistent with the subjective perception of human eyes. The structure information is defined by brightness l, contrast c, and structure attribute s. It is measured by means μ_x and μ_y, standard deviations δ_x and δ_y, and

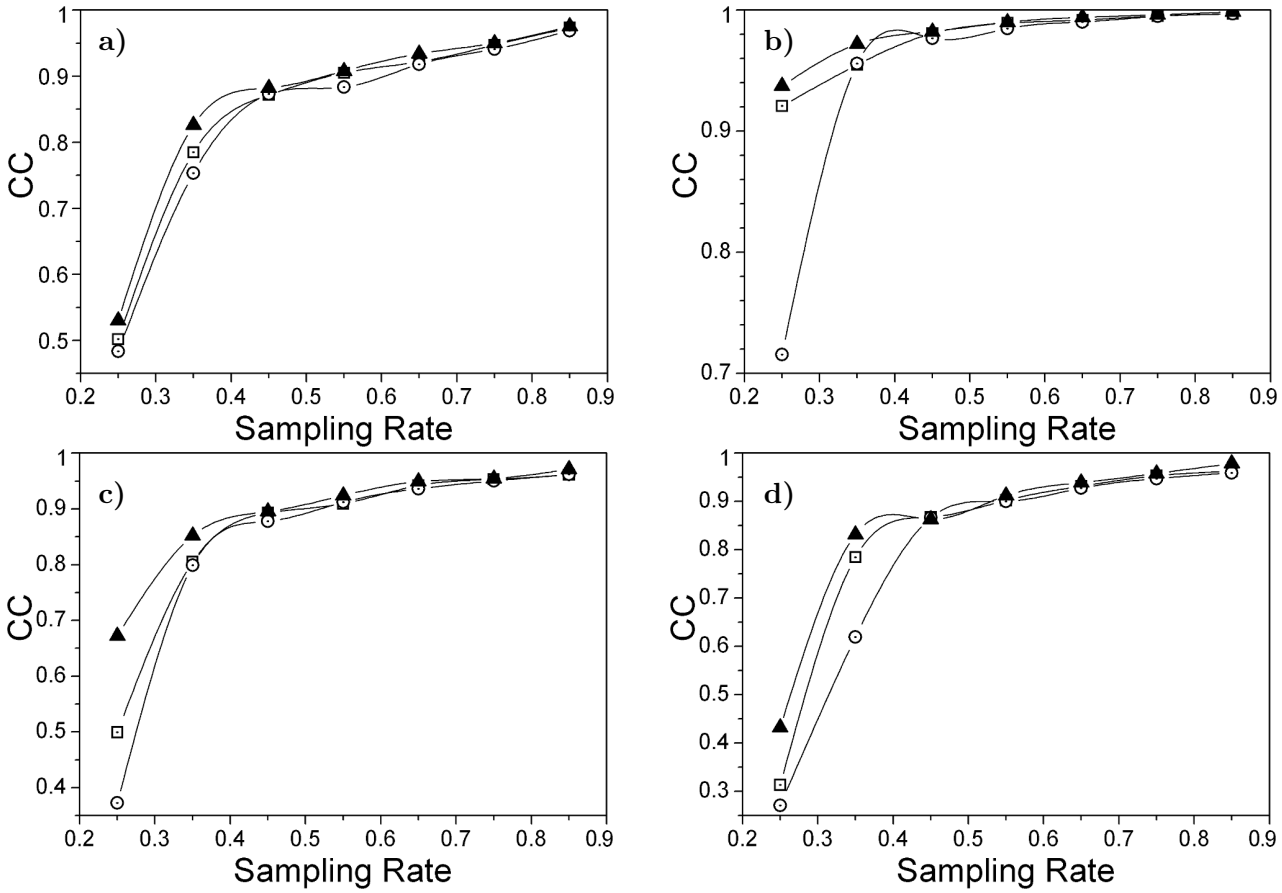

Fig. 5. Comparison of CC values of imaging results with Picture A (a), Picture B (b), Picture C (c), and Picture D (d). Here, the left-eye camera (□), the right-eye camera (⊙), and the binocular camera (▲).

covariance δ_{xy}. The calculation formulas read

$$\begin{cases} l(x,y) = \dfrac{2\,\mu_x\mu_y + C_1}{\mu_x^2 + \mu_y^2 + C_1}\,, \qquad c(x,y) = \dfrac{2\,\delta_x\delta_y + C_2}{\delta_x^2 + \delta_y^2 + C_2}\,, \qquad s(x,y) = \dfrac{\delta_{xy} + C_3}{\delta_x\delta_y + C_3}\,, \\ \mu_x = \bar{x} = \dfrac{1}{N}\sum\limits_{i=1}^{N} x_i, \qquad \mu_y = \bar{y} = \dfrac{1}{N}\sum\limits_{i=1}^{N} y_i, \\ \delta_x = \left[\dfrac{1}{N-1}\sum\limits_{i=1}^{N}(x_i - \bar{x})^2\right]^{1/2}, \qquad \delta_y = \left[\dfrac{1}{N-1}\sum\limits_{i=1}^{N}(y_i - \bar{y})^2\right]^{1/2}, \qquad \delta_{xy} = \dfrac{1}{N-1}\sum\limits_{i=1}^{N}(x_i - \bar{x})(y_i - \bar{y}), \\ \mathrm{SSIM} = l(x,y)\cdot c(x,y)\cdot s(x,y) = \dfrac{(2\,\mu_x\mu_y + C_1)(2\,\delta_{xy} + C_2)}{(\mu_x^2 + \mu_y^2 + C_1)(\delta_x^2 + \delta_y^2 + C_2)}\,, \end{cases} \tag{10}$$

where C_1, C_2, and C_3 represent small positive numbers.

Table 1. Comparison of SSIM Values of Imaging Results.

Sampling Rate		**25%**	**35%**	**45%**	**55%**	**65%**	**75%**	**85%**
Picture A	Left-eye Camera	0.2889	0.4619	0.6577	0.7029	0.8409	0.9581	0.9640
	Right-eye Camera	0.3035	0.4876	0.6722	0.7260	0.8406	0.9639	0.9686
	Binocular camera	0.4292	0.5198	0.6864	0.7267	0.8520	0.9643	0.9769
Picture B	Left-eye Camera	0.4143	0.7064	0.9291	0.9570	0.9826	0.9913	0.9961
	Right-eye Camera	0.5073	0.7233	0.9357	0.9642	0.9909	0.9950	0.9969
	Binocular camera	0.7375	0.7986	0.9598	0.9872	0.9923	0.9957	0.9982
Picture C	Left-eye Camera	0.2027	0.4805	0.7632	0.8965	0.9255	0.9499	0.9650
	Right-eye Camera	0.2589	0.5173	0.7616	0.8956	0.9237	0.9448	0.9569
	Binocular camera	0.3241	0.5151	0.8589	0.9068	0.9282	0.9540	0.9705
Picture D	Left-eye Camera	0.1678	0.2961	0.4766	0.6999	0.8350	0.9508	0.9614
	Right-eye Camera	0.1969	0.3067	0.4942	0.7172	0.8407	0.9543	0.9595
	Binocular camera	0.2703	0.3499	0.5940	0.7243	0.8450	0.9576	0.9725

In Table 1, one can see that

(1) With increase in the sampling rate, the SSIM value shows an upward trend. For example, in the reconstruction process of target (Picture A) where the proposed scheme is used, one can see that, when the sampling rate is 25%, the SSIM value of reconstructed image is 0.4292, when the sampling rate is 55%, the SSIM value is 0.7267, and when the sampling rate is 85%, the SSIM value is 0.9769. In the reconstruction process of target (Picture D) where the proposed scheme is used, one can see that, when the sampling rate is 25%, the SSIM of the reconstructed image is 0.2703, when the sampling rate is 55%, the SSIM is 0.7243, and when the sampling rate is 85%, the SSIM is 0.9725. In other words, no matter what kind of target image is reconstructed, the larger the sampling rate, the larger the SSIM value, and the closer the reconstructed image is to the ideal image.

(2) On the whole, the SSIM value of the image reconstructed by binocular vision fusion is larger than that of the image reconstructed by the left-eye camera and the right-eye camera. For example, in the reconstruction process of the target (Picture C), one can see that, when the sampling rate is 25%, the information entropy SSIM value of the image reconstructed by binocular camera fusion is 0.3241, when the sampling rate is 55%, the SSIM is 0.9068, and when the sampling rate is 85%, the SSIM is 0.9705. When the sampling rate is 25%, the image SSIM values of the left-eye camera and the right-eye camera are 0.2027 and 0.2589, when the sampling rate is 55%, the SSIM values are 0.8965 and 0.8956, and when the sampling rate is 85%, the SSIM values are 0.9650 and 0.9569. The former has higher SSIM value and higher image quality than the latter two single-camera imaging. The results show that the reconstructed image is closer to the ideal image information.

3.3. Information Entropy

The concept of information entropy was first proposed by C. E. Shannon, American engineer. In the field of image, information entropy can directly represent the amount of information contained in an

image. The larger the information entropy value, the more information is contained in an image, the higher the image quality. The calculation formula for information entropy (IE) reads

$$\mathrm{IE} = -\sum_{i=1}^{k} p_i \log_2(p_i), \tag{11}$$

where the unit information entropy is bit/character, k; $0 \leq k \leq 255$ represents the gray level of the image, and p_i represents the probability of occurrence of each gray level.

Table 2. Comparison of IE Values of Imaging Results.

Sampling Rate		**25%**	**35%**	**45%**	**55%**	**65%**	**75%**	**85%**
Picture A	Left-eye Camera	5.6869	6.3656	6.3925	6.6229	7.5063	7.9682	8.6115
	Right-eye Camera	5.5982	5.1538	6.3412	6.7191	7.4492	8.0356	8.5837
	Binocular camera	5.7898	6.3816	6.4241	6.8315	7.5677	8.1013	8.7409
Picture B	Left-eye Camera	5.0871	6.1838	6.2029	6.8409	7.9993	8.6136	8.9714
	Right-eye Camera	5.9415	6.1768	6.2345	6.8725	7.9894	8.7021	9.0916
	Binocular camera	6.1838	6.2299	6.3581	6.9052	8.0398	8.7941	9.1193
Picture C	Left-eye Camera	5.2303	5.9341	6.4725	6.9522	7.9635	8.6734	8.9881
	Right-eye Camera	5.6102	5.9069	6.6894	6.9805	7.9300	8.6425	8.9700
	Binocular camera	5.7302	6.2577	6.8894	7.5806	8.015	8.8350	9.0017
Picture D	Left-eye Camera	5.5421	6.6914	6.6909	6.9044	7.7112	8.1614	8.7881
	Right-eye Camera	5.8501	5.9295	6.6334	6.9510	7.7229	8.2484	8.7817
	Binocular camera	6.3452	6.6613	6.7161	6.9202	7.7368	8.3248	8.9588

In Table 2, one can see that

(1) With increase in the sampling rate, the IE value shows an upward trend. For example, in the reconstruction process of target (Picture A) where the proposed scheme is used, one can see that the IE value of reconstructed image is equal to 5.7898, when the sampling rate is 25%, it is equal to 6.8315, when the sampling rate is 55%, and it is equal to 8.7409, when the sampling rate is 85%. In the reconstruction process of the target (Picture D) where the proposed scheme is used, one can see that the IE value of the reconstructed image is equal to 6.3452 when the sampling rate is 25%, and it is equal to 6.9202, when the sampling rate is 55%, and it is equal to 8.9588, when the sampling rate is 85%. In other words, no matter what kind of target image is reconstructed, the larger the sampling rate, the larger the IE value, the more information is contained in the image, and the higher the image quality.

(2) On the whole, the image IE value of binocular vision fusion reconstruction scheme is larger than that of the left-eye camera and the right-eye camera imaging. For example, in the reconstruction process of target (Picture C), one can see that, when the sampling rate is 25%, the information entropy (IE) value of binocular camera fusion reconstruction image is 5.7302, and when the sampling rate is 55%, the IE value is 7.5806. When the sampling rate is 85%, the IE value is 9.0017. The image IE values of the left-eye camera and the right-eye camera are 5.2306 and 5.6102, when the sampling rate is 25%; it is equal to 6.9522 and 6.9805, when the sampling rate is 55% and 8.9881, while it is equal to 8.9700, when the sampling rate is 85%. The former contains more information than the latter two (the left-eye camera

and the right-eye camera) imaging and has higher imaging quality. The results obtained show that the scheme has better quality of image, which proves that the scheme is more effective in the information entropy evaluation index.

3.4. Root Mean Square Error and Peak Signal-to-Noise Ratio

The root mean squared error (RMSE) is used to measure the fidelity of the reconstructed image, and its main purpose is to calculate the relationship between the reconstructed image and the ideal image. If the RMSE value is relatively small, it indicates that the reconstructed image is close to the ideal image, which reflects that the evaluation effect of the method is better. The peak signal-to-noise ratio (PSNR) is used to analyze the robustness of reconstructed images. The larger the PSNR value, the higher the quality of the reconstructed image. The calculation formulas read

$$\mathrm{RMSE} = \sqrt{\frac{\sum_{i=1}^{M}\sum_{j=1}^{N}(V_{i,j}-V'_{i,j})^2}{M\times N}}, \quad \mathrm{MSE} = \frac{\sum_{i=1}^{M}\sum_{j=1}^{N}(V_{i,j}-V'_{i,j})^2}{M\times N}, \quad \mathrm{PSNR} = 10\lg\frac{V_{\max}^2}{\mathrm{MSE}}, \quad (12)$$

where $M \times N$ represents the size of the image, $V_{i,j}$ and $V'_{i,j}$ represent the pixel values of the original image and the reconstructed image, respectively, and MSE stands for mean square error.

Table 3. Comparison of RMSE Values in Imaging Results.

Sampling Rate		**25%**	**35%**	**45%**	**55%**	**65%**	**75%**	**85%**
Picture A	Left-eye Camera	7.0170	6.2792	5.5224	3.9368	2.7330	1.3663	1.1006
	Right-eye Camera	7.1397	6.4161	5.6703	4.2048	2.7396	1.4728	1.0588
	Binocular camera	6.8298	6.0058	5.3841	3.9293	2.1730	1.2589	0.9023
Picture B	Left-eye Camera	6.5269	5.8068	4.3196	3.0687	1.8125	0.6029	0.381
	Right-eye Camera	6.4126	5.7646	4.2225	2.9711	1.7362	0.5887	0.4527
	Binocular camera	6.0970	5.4952	4.2062	2.5640	1.2507	0.4617	0.2128
Picture C	Left-eye Camera	7.7168	6.6290	4.8704	2.5218	1.8497	1.3775	0.8868
	Right-eye Camera	7.9917	6.8751	4.8979	2.5230	1.7663	1.3606	0.9433
	Binocular camera	7.0849	6.3191	4.9369	2.3826	1.5994	1.1005	0.5632
Picture D	Left-eye Camera	6.8885	5.9227	4.1942	2.9485	2.0464	1.4487	1.1891
	Right-eye Camera	6.5157	5.9775	4.3594	3.1293	1.9145	1.3986	1.1361
	Binocular camera	6.0450	5.3041	4.0898	2.8509	1.8861	1.2955	0.9045

In Table 3, one can see that

(1) With increase in the sampling rate, the RMSE value shows a downward trend. For example, in the reconstruction process of target (Picture A) where the proposed scheme is used, one can see that, when the sampling rate is 25%, the RMSE value of the reconstructed image is equal to 6.8298, when the sampling rate is 55%, the RMSE value is equal to 3.9293, and when the sampling rate is 85%, the RMSE value is equal to 0.9023. In the reconstruction process of the target (Picture D), one can see that the RMSE value of the reconstructed image is equal to 6.0450, when the sampling rate is 25%, and it is equal to 2.8509, when the sampling rate is 55%, and it is equal to 0.9045 when the sampling rate is 85%.

In other words, the larger the sampling rate, the smaller the RMSE value, and the higher the fidelity between the reconstructed image and the ideal image.

(2) On the whole, the RMSE value of binocular vision fusion reconstruction scheme is larger than that of the left-eye camera and the right-eye camera imaging. For example, in the reconstruction process of target (Picture C), one can see that, when the sampling rate is 25%, the information entropy RMSE value of binocular camera fusion reconstruction image is equal to 7.0849. The RMSE value is equal to 2.3826, when the sampling rate is 55%, and it is equal to 0.5632, when the sampling rate is 85%. When the sampling rate is 25%, the image RMSE values of the left-eye camera and the right-eye camera are 7.7168 and 7.9917, respectively. When the sampling rate is 55%, the RMSE values are equal to 2.5218 and 2.5230, and when the sampling rate is 85%, the RMSE values are equal to 0.8868 and 0.9433, respectively. The RMSE of the former is smaller than that of the latter two; that is, the imaging quality is higher. The results obtained show that the proposed scheme has better imaging fidelity.

Table 4. Comparison of PSNR Values in Imaging Results.

	Sampling Rate	**25%**	**35%**	**45%**	**55%**	**65%**	**75%**	**85%**
Picture A	Left-eye Camera	9.8296	13.3778	15.5172	18.1811	21.2394	28.6853	32.7685
	Right-eye Camera	10.0395	13.7331	16.0121	18.3067	20.2724	29.3375	33.2160
	Binocular camera	10.3698	14.4891	17.5020	19.3402	25.1139	30.1847	34.2035
Picture B	Left-eye Camera	10.9323	18.9102	21.6396	23.4714	26.8515	29.4437	34.4064
	Right-eye Camera	16.3987	19.1155	22.3037	24.3034	26.7083	29.6512	34.9325
	Binocular camera	17.6162	21.5544	23.4200	26.3665	28.5391	30.0582	36.2284
Picture C	Left-eye Camera	7.1567	11.2888	15.8069	17.0099	20.3342	28.6551	29.7343
	Right-eye Camera	7.5052	12.8527	14.8896	17.0142	21.4009	28.0524	30.6031
	Binocular camera	10.3634	14.6281	16.6906	19.5073	25.6067	29.4368	31.5042
Picture D	Left-eye Camera	9.2164	14.5715	17.5923	21.4838	26.3656	30.5345	31.5315
	Right-eye Camera	10.2649	14.7327	17.2228	20.2546	27.7179	30.8289	32.5443
	Binocular camera	12.3505	16.7351	19.2404	23.7010	29.0419	31.1535	33.5027

In Table 4, one can see that

(1) With increase in the sampling rate, the PSNR value shows an upward trend. For example, in the reconstruction process of target (Picture A) where the proposed scheme is used, one can see that, when the sampling rate is 25%, the PSNR value of the reconstructed image is equal to 10.3698, and when the sampling rate is 55%, the PSNR value is equal to 19.3402. When the sampling rate is 85%, the PSNR value is equal to 34.2035. During the reconstruction of target (Picture D), one can see that, when the sampling rate is 25%, the PSNR value of the reconstructed image is equal to 12.3503. Also, when the sampling rate is 55%, the PSNR value is equal to 23.7010, and, when the sampling rate is 85%, the PSNR value is equal to 33.5027. In other words, no matter what kind of target image reconstruction, the larger the sampling rate, the larger the PSNR value, the higher the image quality.

(2) On the whole, the PSNR value of the image with binocular vision fusion reconstruction scheme is larger than that of the image with the left-eye camera and the right-eye camera. For example, in the reconstruction process of the target (Picture C), one can see that, when the sampling rate is 25%, the

information entropy PSNR value of the reconstructed image with binocular camera fusion is equal to 10.3634. When the sampling rate is 55%, the PSNR value is equal to 19.5073, and, when the sampling rate is 85%, the PSNR value is equal to 31.5042. When the sampling rate is 25%, the PSNR values of left-eye camera and right-eye camera are equal to 7.1567 and 7.5052, respectively. When the sampling rate is 55%, the PSNR values are equal to 17.0099 and 17.0142, and, when the sampling rate is 85%, the PSNR values are equal to 29.7343 and 30.6031. Under the same sampling conditions, the former has a larger PSNR value than the latter two single-camera imaging, and the imaging quality is higher. The results obtained show that the scheme has better robustness.

3.5. Bit Error Rate

In the process of image information transmission, due to the existence of various factors, errors often occur, resulting in error codes. The bit error rate (BER) is generally expressed in scientific notation, and the lower the BER, the better. The calculation formula reads

$$\mathrm{BER} = \frac{\text{Error bit rate}}{\text{Total bit rate}} \cdot 100\% \,. \tag{13}$$

In Fig. 6, we show the comparison of BER values of the imaging results of the four target images selected in this study of the left-eye camera, the right-eye camera, and binocular camera at different

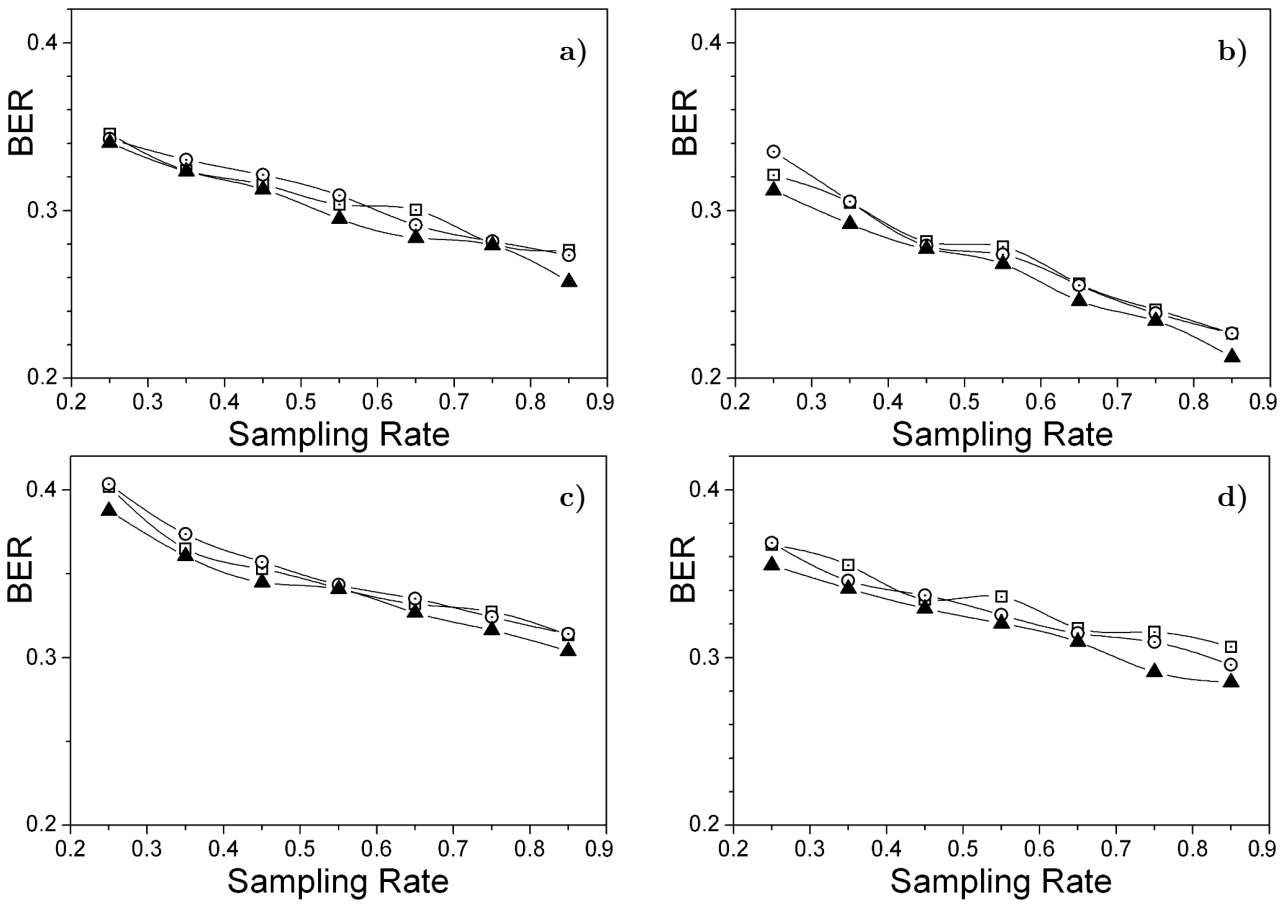

Fig. 6. Comparison of BER values of imaging results; here, Picture A (a), Picture B (b), Picture C (c), and Picture D (d). Here, the left-eye camera (□), the right-eye camera (⊙), and the binocular camera (▲).

sampling rates. Here, the gray curve and the red curve represent the BER value changes of reconstructed images of the left-eye camera and the right-eye camera, respectively, and the blue curve represents the BER value changes of reconstructed images of binocular camera fusion. The curve change trend demonstrates that

(1) With increase in the sampling rate, the BER value becomes smaller and smaller; that is, the imaging quality becomes higher and higher.

(2) For any kind of target image, the BER value of the binocular vision fusion imaging based on the proposed scheme is lower than that of the imaging BER of the left-eye camera and the right-eye camera, so the imaging quality is better and closer to the ideal image information.

4. Conclusions

In order to satisfy the visual characteristics of human eyes and promote the development of imaging field, in this paper, we proposed a ghost imaging method based on binocular vision matching fusion. First, we simulated the imaging process of binocular vision by ghost imaging algorithm. By the SURF algorithm, feature points of the collected sub-images were extracted, and feature point matching was performed to obtain coordinate values of matching points. Finally, the NSML fusion algorithm was used to fuse the registered images of two sub-images to obtain a high-resolution image. Whether from the visual (human vision) or objective analysis (CC, SSIM, IE, RMSE, PSNR, BER, etc.), we proved that the proposed scheme had better imaging quality, better fidelity and robustness, and the reconstructed image was closer to the ideal image. It also provides a new method for binocular vision imaging technology, which has a good theoretical basis and application prospect.

Acknowledgments

The authors are indebted to the anonymous referees for their instructive comments and suggestions. We are very thankful for the participants for their support and contribution to this study.

References

1. L. Zhu, Y. Zhang, Y. Wang, and C. Cheng, *Comput. Mater. Contin.*, **71**, 593 (2022); DOI: 10.32604/cmc.2022.022053
2. X. Tian, R. Liu, Z. Wang, et al., *Inf. Fusion*, **77**, 19 (2022); DOI: 10.1016/j.inffus.2021.07.002
3. D. Lin, Z. Wang, H. Shi, et al., *J. Phys. Conf. Ser.*, **1738**, 012033 (2021).
4. L. Liu, *J. Surv. Eng.*, **147**, 04021017 (2021).
5. Z. Xiao, W. Zhang, L. Geng, et al., *Opto-Electron. Eng.*, **41**, 6 (2014).
6. L. Yang, B. Wang, R. Zhang, et al., *IEEE Photon. J.*, **10**, 7800316 (2018).
7. C. Bi, X. Hao, M. E, et al., *Aviat. Pr. Man. Technol.*, **56**, 2 (2020).
8. F. Fooladgar, S. Samavi, S. Soroushmehr, et al., *IEEE Sens. J.*, **13**, 4236 (2013).
9. Z. Yang, S. Yuan, J. Li, et al., *J. Opt.*, **24**, 065702 (2022).
10. W. Zhang, D. Yu, Y. Han, et al., *Opt. Lasers Eng.*, **148**, 106769 (2022); DOI: 10.1016/j.optlaseng.2021.106769
11. W. Yu, N. Wei, Y. Li, et al., *Opt. Lasers Eng.*, **155**, 107067 (2022).
12. Y. Hualong and G. Daidou, *Opt. Lasers Eng.*, **171**, 107790 (2023); DOI: 10.1016/j.optlaseng.2023.107790
13. D. Klyshko, *Phys. Lett. A*, **128**, 133 (1988).
14. J. Shapiro, *Phys. Rev. A*, **78**, 061802 (2008).

15. C. Luo and J. Cheng, *Opt. Lett.*, **38**, 5381 (2013).
16. Z. Zhang, X. Ma, and J. Zhong, *Nat. Commun.*, **6**, 6225 (2015); DOI: 10.1038/ncomms7225
17. D. Shi, J. Zhang, J. Huang, et al., *Opt. Lasers Eng.*, **102**, 100 (2018); DOI: 10.1016/j.optlaseng.2017.10.022
18. L. Zhang, H. Ye, D. Zhang, et al., *Appl. Phys. B*, **125**, 57 (2019).
19. H. Ye, Y. Kang, J. Wang, et al., *J. Korean Phys. Soc.*, **80**, 964 (2022).
20. S. Liu, X. Meng, Y. Yin, et al., *Opt. Lasers Eng.*, **147**, 106744 (2021); DOI: 10.1016/j.optlaseng.2021.106744
21. M. Hou and C. Hou, *Laser Optoelectron. Prog.*, **60**, 0200003 (2023).
22. H. Guo, L. Wang, and S. Zhao, *Chin. Phys. B*, **31**, 084201 (2022).
23. X. Chen, *J. Appl. Mat. Phys.*, **010**, 1098 (2022).
24. H. Ye, L. Zhang, and D. Zhang, *Opt. Laser Technol.*, **137**, 106779 (2021); DOI: 10.1016/j.optlastec.2020.106779
25. P. Ryczkowski, C. Amiot, J. Dudley, et al., *Sci. Rep.*, **11**, 8403 (2021).
26. X. Qu, J. Yan, and G. Yang, *Opt. Pr. Eng.*, **17**, 1203 (2009).